Nano Research

ISSN 1998-0124 CN 11-5974/O4
https://doi.org/10.1007/s12274-022-4146-4

Research Article

# N-doped $MoS_2$ via assembly transfer on an elastomeric substrate for high-photoresponsivity, air-stable and stretchable photodetector

Shuyan Qi[1,§], Weifeng Zhang[1,§], Xiaoli Wang[1], Yifan Ding[2], Yan Zhang[1], Jiakang Qiu[1], Ting Lei[3], Run Long[1], and Nan Liu[1] (✉)

[1] *Beijing Key Laboratory of Energy Conversion and Storage Materials, College of Chemistry, Beijing Normal University, Beijing 100875, China*
[2] *Beijing National Laboratory for Molecular Sciences (BNLMS), Key Laboratory of Polymer Chemistry and Physics of Ministry of Education, Center of Soft Matter Science and Engineering, College of Chemistry and Molecular Engineering, Peking University, Beijing 100871, China*
[3] *Department of Materials Science and Engineering, College of Engineering, Peking University, Beijing 100871, China*
[§] *Shuyan Qi and Weifeng Zhang contributed equally to this work.*

© Tsinghua University Press 2022

**Received:** 1 October 2021 / **Revised:** 7 January 2022 / **Accepted:** 11 January 2022

## ABSTRACT

As a direct-bandgap semiconductor, single-layer $MoS_2$ has gained great attention in optoelectronics, especially wearable photodetectors. However, $MoS_2$ exhibits poor photoresponsivity on a stretchable substrate due to intrinsic low carrier density and a large number of scattering centers on polymer substrates. Few air-stable yet strong dopants on $MoS_2$ has been reported. In addition, the roughness, hydrophobicity and susceptibility to organic solvents of polymer surface are critical roadblocks in the development of stretchable high-performance $MoS_2$ photodetectors. Here, we realize a stretchable and stable photodetector with high photoresponsivity by combining n-type dopant ((4-(1,3-dimethyl-2,3-dihydro-1H-benzoimidazol-2-yl) phenyl) dimethylamine, N-DMBI) with $MoS_2$ and assembly transfer technique. It is found electron tends to transfer from N-DMBI to $MoS_2$ and the effect is maintained after the integrable photodetector transferred directly by elastic substrate styrene-ethylene-butylene-styrene (SEBS), even after being exposed to the air for 20 days, which benifits greatly from the encapsulation of SEBS. The increased carrier density greatly promotes carrier injection efficiency and photogenerated electron–hole separation efficiency at the metal–semiconductor interface, thus offering a significantly improved photoresponsivity in $MoS_2$ photodetectors. Moreover, such photodetector shows great durability to stretch, which can remain functional after stretched 100 cycles within its stretch limit. Our strategy opens a new avenue to fabricate high-photoresponsivity stretchable electronics or optoelectronics of two-dimensional (2D) materials.

## KEYWORDS

transition metal dichalcogenides, charge transfer, stretchable photodetectors, organic molecules

## 1 Introduction

Photodetector, a device that converts optical signals into electrical signals, is commonly used for sensing, imaging, and communication, etc. [1, 2]. Recently, it has been continuously required to reduce the feature size to meet the development requirements of miniaturization and to have a certain flexibility to adapt for wearable devices, such as electronic eyes, flexible cameras, ultraviolet (UV) skin sensors and so forth [3–7]. Photodetectors based on traditional photoelectric materials are so hard and brittle that they cannot be applied to wearable devices. In addition, silicon technology has reached the physical limit and cannot keep on Moore's Law. Instead, two-dimensional (2D) materials with atomic thickness are regarded as promising candidates for state-of-the-art optoelectronics due to their outstanding optoelectronic characteristics and mechanical flexibility [8–11]. $MoS_2$ is a prototypical 2D semiconducting material, which has been extensively studied. Similar to the other 2D semiconducting materials, its band gap changes with the number of layers. Bulk $MoS_2$ possesses an indirect band gap of 1.2 eV. As the number of layers decreases, its band gap increases. Particularly, single-layer $MoS_2$ possesses a direct band gap of about 1.8 eV, resulting in much more efficient light absorption and exciton emission. Due to above innate advantages of single-layer $MoS_2$, single-layer $MoS_2$ flexible photodetectors have been demonstrated [12–14]. However, a large number of scattering centers on a polymer substrate and intrinsic low carrier density seriously alleviate their photocurrent and corresponding photoresponsivity.

Doping is an efficient way to modulate carrier concentration and passivate surface defects for advanced electronic and optoelectronic applications [15–21]. Compared with doping methods established by conventional semiconductors, such as substitutional doping, solution processed chemically doping has the advantages of simple operation, mass production and controllable doping. Hybrid systems based on $MoS_2$ and other low-dimensional materials constructed by chemically doping method have been explored to realize high-performance photodetection, whereas there are still few reports on air-stable yet strong dopants. On the other hand, the common processing technology is not

Address correspondence to nanliu@bnu.edu.cn

compatible with elastic substrates, of which the surface is generally rough, hydrophobic and susceptible to organic solvent. An alternative way is to transfer the hybrid system onto the elastic substrate by a carrier, such as polymethyl methacrylate (PMMA). Neverthless, it's still unavoidable to use organic solvents when removing the carrier. Meanwhile, surface adsorbates tend to be taken away by the carrier, which damages the established interface function. Cracks and wrinkles also inevitably occur in PMMA-supporting transfer process. Therefore, an effective strategy to enrich the photoresponsivity of the $MoS_2$ photodetector while being compatible with elastomeric polymer is highly demanded for the development of stretchable photodetectors.

Here, we present an operable way to achieve high-photoresponsivity, air-stable and stretchable photodetectors based on 2D materials. (4-(1,3-Dimethyl-2,3-dihydro-1H-benzoimidazol-2-yl) phenyl) dimethylamine (N-DMBI), a novel air-stable n-dopant, was applied on the single-layer $MoS_2$ to regulate the electron concentration of $MoS_2$ via charge transfer. The integrable N-DMBI doped $MoS_2$ photodetector was transferred in one step with a transparent elastomer, styrene-ethylene-butylene-styrene (SEBS). Because dopants are sandwiched between $MoS_2$ and SEBS, the charge transfer interaction between $MoS_2$ and N-DMBI is maintained after transfer, even after being exposed to the air for 20 days. Because of more efficient carrier injection and photogenerated electron–hole separation at the metal–semiconductor interface, as-fabricated photodetector on SEBS displays a greatly enhanced photoresponsivity of 738 $A \cdot W^{-1}$, almost 100 times increase compared with undoped $MoS_2$. It can also withstand tensile strain as high as 5% when stretched parallel to the direction of current flow, 10% when stretched perpendicular to the direction of current flow, and keep functional after stretched 100 cycles within its stretch limit. These results provide a strong evidence for the application potential possessed by 2D materials for the emergence of high-performance stretchable electronics or optoelectronics.

## 2 Experimental section/methods

### 2.1 Synthesis of single-layer $MoS_2$ films and N-DMBI solutions

Before synthesis of $MoS_2$ films, a piece of molybdenum foil (Alfa-Aesar, 99.95%) was pre-oxidized by electrochemical method. Then, the molybdenum foil was folded in half and stood on a 300 nm $SiO_2$/Si substrate. Subsequently, they were placed on a quartz boat and loaded into the third zone downstream of the 3-zone tube furnace. Another quartz boat with sulfur powder (Alfa Aesar, 99.5%, 1.5 g) was loaded into the first zone. The distance between the two quartz boats was about 18 cm. Next, the third zone was heated up to 750 °C at the rate of 20 $°C \cdot min^{-1}$, and then kept for 30 min under 100 sccm of Ar gas. The temperature of the first zone rose rapidly to 190 °C when the third temperature rose to 650 °C, then maintained 30 min. After the reaction, the furnace was cooled naturally with 200 sccm of Ar gas. N-DMBI was synthesized according to Ref. [22]. To prepare different concentrations of N-DMBI solution, 2, 5 and 10 mg of N-DMBI were dissolved in 2 g chlorobenzene ($C_6H_5Cl$), respectively.

### 2.2 Device fabrication

To fabricate pristine $MoS_2$ field-effect transistors (FETs), as-prepared $MoS_2$ films were transferred on another 300 nm $SiO_2$/Si substrate with specific markers. Typical E-beam lithography (EBL) procedures were employed to define electron patterns. Au (50 nm) was thermally deposited followed by lift-off process to make the electrical contact. Finally, the devices were heated at 150 °C for 30 min in the glovebox to remove impurities. For N-DMBI doped $MoS_2$ FETs, the pristine $MoS_2$ FETs were spin-coated by N-DMBI solutions at 2,000 rpm for 30 s in the glovebox. Then, the FETs were dried at 150 °C for 20 min.

### 2.3 Preparation of SEBS films and transfer process for stretchable photodetectors

SEBS films were prepared by dissolving 1.8 g of SEBS in 15 mL of toluene ($C_7H_8$), stirring at room temperature for 1 h and dropping on glass slides to form films until there were no bubbles in solution. The transfer process involves tearing the SEBS film off the glass slide, sticking the sticky side tightly to devices on the silicon substrate, pressing firmly and soaking in the alkaline solution. After a few minutes, the film was separated from the silicon substrate and floated on the liquid surface. It was then taken out, rinsed with deionized water and blow dried with $N_2$.

### 2.4 Material and device characterization

Optical microscope (OM) (Leica, DM2700M), atomic force microscope (AFM) (Digital Instrument, NanoScope IIIA MultiMode), Raman and photoluminescence (PL) spectroscopy (Horiba, LabRAM HR Evolution), and X-ray photoelectron spectroscopy (XPS) (Thermo Fisher, ESCALAB 250Xi) were used for material characterization. The excitation wavelength for Raman and PL measurements was 532 nm.

The Si peak at 520.7 $cm^{-1}$ was used for calibration in the Raman and PL spectra. Raman and PL mapping images were collected at the step of 1.5 and 3 μm, respectively. All electrical and optoelectronic measurements were performed using a source measure unit (Keithley, 2636B). A xenon lamp was used as light source for photodetection and the wavelength of the incident light was modulated by the monochromator.

### 2.5 Density functional theory (DFT) calculations

The DFT calculations were performed with the Vienna *ab initio* simulation package (VASP) [23]. The Perdew–Burke–Ernzerhof (PBE) [24] functional was chosen to describe electron exchange–correlation energy and the projector-augmented wave [25] approach was used to treat the interactions between the ionic cores and valence electrons. The van der Waals interactions were considered with the Grimme DFT-D3 method [26]. The periodic interface was represented by a slab model containing a single-layer ($5 \times 5 \times 1$) $MoS_2$ supercell and an optimized N-DMBI radical (N-DMBI·). The optimization of the N-DMBI· was performed by using M062X/6-31G** method [27] with same parameters as in the previous work [28]. A 15 Å vacuum region was added to avoid the spurious interaction between other layers. To realize the convergence of energy and wave function, the geometry relaxation stopped when the ion forces were less than $10^{-3}$ $eV \cdot Å^{-1}$ with the plane-wave basis cutoff energy of 400 eV. All systems were relaxed at 0 K using a $5 \times 5 \times 1$ Γ-centered *k*-point Monhorst–Pack mesh for electronic structure calculations using denser $10 \times 10 \times 1$ *k*-mesh [29]. After that, band structure was obtained using line-mode along Γ-M-K-Γ path with 50 *k*-points between two adjacent high-symmetric *k*-point.

## 3 Results and discussion

N-DMBI molecule is a novel n-type dopant, which is typically activated to form N-DMBI· that can efficiently donate electrons to organic semiconductors and promote the carrier density of materials [30, 31], providing a possible strategy to enhance the photoresponsivity of $MoS_2$ photodetector. Bearing this in mind,

we performed DFT calculations to obtain electronic structure of the single-layer $MoS_2$ and $MoS_2$/N-DMBI· system. The calculated band structure shows that compared with the pristine single-layer $MoS_2$ (Fig. 1(a)), the electron donor state provided by the N-DMBI· is closer to conduction band edge of $MoS_2$ together with the lifted Fermi level in the $MoS_2$/N-DMBI· system (Fig. 1(b)), indicating an n-type doping. The calculated charge densities of N-DMBI· lowest unoccupied molecular orbital (LUMO) (Fig. 1(c)) and $MoS_2$ conduction band minimum (CBM) (Fig. 1(d)) indeed show that the electron donor state is delocalized over the entire N-DMBI· while the acceptor states are uniformly localized on the Mo atom of $MoS_2$ sheet. The planar N-DMBI· can enhance the donor–acceptor interaction, facilitating transfer of electrons from the N-DMBI· to the $MoS_2$, as shown in Fig. 1(e) where charge

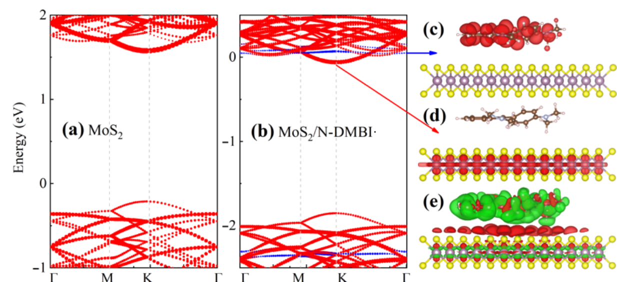


**Figure 1** Theoretical understanding of N-DMBI· doping on single-layer $MoS_2$. Band structures of (a) pristine single-layer $MoS_2$ and (b) $MoS_2$/N-DMBI system. Panels (c) and (d) show the charge densities of the electron donor state (LUMO of N-DMBI·) and acceptor state (CBM of $MoS_2$) in the $MoS_2$/N-DMBI· system, corresponding to the energy levels marked by the blue and red arrow lines in (b). Panel (e) shows the charge density difference between $MoS_2$/N-DMBI· system and isolated components. Red and green colors represent charge accumulation and depletion region, respectively.

depletion in the N-DMBI· is accompanied by charge accumulation in the $MoS_2$. In order to test the influence of the N-DMBI· aggregations on the electronic properties of the $MoS_2$/N-DMBI·, we calculated the band structure and charge densities of a single-$MoS_2$ interfaced with an N-DMBI· dimer (Fig. S1 in the Electronic Supplementary Material (ESM)). The results are consistent with the data shown in Fig. 1, demonstrating that the minor difference arises from the $MoS_2$/N-DMBI· dimer created two degenerated donor states localized above the $MoS_2$ CBM, and indicating that N-DMBI· aggregations generally increase the number of electron donor states while the fundamental electronic properties maintain. In addition, to investigate the effect of N-DMBI doping on $MoS_2$ band structure, we performed ultraviolet photoelectron spectroscopy (UPS) characterization. After N-DMBI doping, the work function ($\phi$) and Fermi level are all decreasing compared with the pristine $MoS_2$. The Fermi level shifts closer to the CBM (Fig. S2 in the ESM). The results suggest $MoS_2$ decorated by N-DMBI· provides an excellent n-type doping semiconductor and encourage us to proceed following experiments for realizing high-photoresponsivity $MoS_2$ photodetectors.

We next applied N-DMBI on single-layer $MoS_2$ and evaluated the effectiveness of doping by spectroscopic characterizations and electrical measurements. Single-layer $MoS_2$ films were synthesized by chemical vapor deposition (CVD) on a $SiO_2$/Si substrate with electrochemically oxidized Mo foil and sulfur powder as precursors. To achieve N-DMBI doping, N-DMBI solution was spin-coated on the surface of $MoS_2$ followed by baking to remove excess solvent (see Experimental section/methods). OM and AFM images of $MoS_2$ before and after N-DMBI doping are shown in Fig. 2(a). Before doping, the large triangle $MoS_2$ exhibits a smooth surface with a thickness of about 0.7 nm, which suggests as-grown

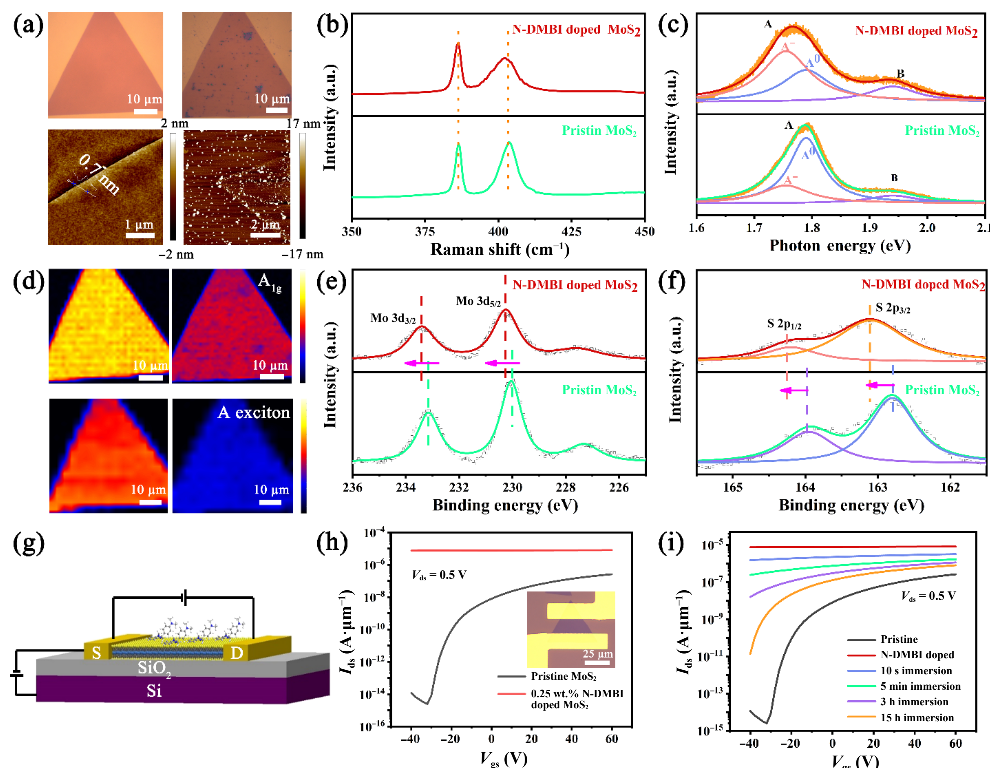


**Figure 2** Characterization of N-DMBI doping on single-layer $MoS_2$. (a) Optical and AFM images of single-layer $MoS_2$ before (left) and after N-DMBI doping (right). (b) Raman, (c) PL spectra and (d) Raman mapping images (top) corresponding to $A_{1g}$, PL mapping images (bottom) corresponding to A exciton of the single-layer $MoS_2$ before and after N-DMBI doping. XPS spectra of (e) Mo 3d and (f) S 2p peaks of $MoS_2$ before and after N-DMBI treatment. Dash lines: experimental data. Solid lines: fitting curves. (g) Schematic illustration of a back-gated $MoS_2$ FET used for N-DMBI/$MoS_2$ interface doping studies. (h) The representative transfer curves of $MoS_2$ FETs before (black curve) and after (red curve) N-DMBI doping. The inset is an optical image of a $MoS_2$ FET on a $SiO_2$/Si substrate. (i) Transfer characteristic curves of the $MoS_2$ FET before doping (black), after N-DMBI doping immediately (red) and immersed in chlorobenzene for different time (blue for 10 s, green for 5 min, purple for 3 h and yellow for 15 h).

$MoS_2$ would be crystalline single-layer $MoS_2$. After doping, N-DMBI distributes on the surface of $MoS_2$ and forms into aggregates ranging from 10–30 nm in diameter, resulting in a rougher $MoS_2$ surface. We speculate that the size and density of N-DMBI aggregates can be controlled by the spin-coating speed or the concentration of N-DMBI solution.

Raman and PL spectroscopy were carried out to examine the quality of $MoS_2$ and explore the electronic interaction between $MoS_2$ and N-DMBI. As shown in Fig. 2(b), two characteristic Raman peaks appear at 386 and 404 $cm^{-1}$ for pristine $MoS_2$, corresponding to the $E^1_{2g}$ (in-plane vibration of Mo and S atoms) and $A_{1g}$ (out-of-plane vibration of S atoms) photon modes respectively. Their difference of frequency is ~ 18 $cm^{-1}$ and the full width at half-maximum (FWHM) of $E^1_{2g}$ is ~ 4 $cm^{-1}$, which infers as-grown $MoS_2$ is single-layer with high quality and few defects [32]. After N-DMBI doping, there is almost no change in the $E^1_{2g}$ peak, while $A_{1g}$ peak shows an obvious red-shift of 1–2 $cm^{-1}$ (Fig. S3 in the ESM), accompanied with the FWHM of the $A_{1g}$ peak increasing from 4–5 to 7–8 $cm^{-1}$ (Fig. S4 in the ESM). Raman mapping images prove that this change is not a special case. This is consistent with the previously reported phenomenon of n-doped $MoS_2$, which infers that electrons are transferred from N-DMBI to $MoS_2$ [33–35]. Figure 2(c) shows the PL spectra of pristine $MoS_2$ and N-DMBI doped $MoS_2$. Generally, there are two PL emission peaks for single-layer $MoS_2$, where A and B peaks locate at ~ 1.80 and ~ 1.94 eV, related to the direct radiative recombination of A and B excitons respectively. After N-DMBI doping, there is an apparent red-shift in peak position and reduction in peak intensity on the A peak. To get more information about the charge transfer from N-DMBI to $MoS_2$, the A peak was deconvolved into two components, negatively charged trion ($A^-$) peak and neutral exciton ($A^0$) peak [36], corresponding to the trion and the exciton radiative recombination, respectively. Fitting analysis shows that the $A^-/A^0$ intensity ratio of N-DMBI doped $MoS_2$ substantially rises compared with that of pristine $MoS_2$, which means the concentration of excitons dropped sharply. It can be explained by the electron transfer from N-MDBI to $MoS_2$ and the binding of excess electrons with photogenerated electron–hole pairs [34, 37]. Moreover, the lower radiative recombination efficiency of trions can be attributed to the reduction in A peak intensity [38]. The intensity mappings on the A exciton peak in PL show obvious decreases and the distributions are quite uniform except for some dark spots at N-DMBI aggregates (Fig. 2(d) left vs. right). The color changes in the intensity mappings suggest that the N-DMBI doping effect is uniformly distributed over the whole single crystalline $MoS_2$ domain.

We also performed XPS measurements to investigate the effects of N-DMBI on chemical structure and energy level of $MoS_2$. As shown from the spectra of Mo 3d and S 2p core levels in Figs. 2(e) and 2(f), both the binding energy of Mo 3d and S 2p peak shifts to higher energy side with shift value of ~ 0.3 and ~ 0.2 eV respectively after N-DMBI doping on $MoS_2$. As the binding energy is directly correlated with the electron density, this blue-shift reveals the rise of Fermi level upon n-doping of $MoS_2$, which again confirms there is electron transfer at the interface of $MoS_2$/N-DMBI [34, 39].

The effectiveness of N-DMBI doping was further proved by electrical characterizations. Electrode contacts of single crystalline $MoS_2$ FETs were defined by EBL followed by thermal evaporation and lift-off techniques (see Experimental section/methods). Figure 2(g) shows the schematic illustration of a $MoS_2$ FET (channel length: 15 μm; channel width: depending on the size of the sample). From the representative transfer curve (Fig. 2(h)), the pristine $MoS_2$ FET exhibits n-type semiconductor behavior. The drain current ($I_{ds}$) is effectively regulated by the gate voltage ($V_{gs}$), with the mobility of 15.5 $cm^2 \cdot V^{-1} \cdot s^{-1}$, on/off current ratio of around $10^8$ and the threshold voltage ($V_{th}$) of 15.6 V at source-drain voltage ($V_{ds}$) of 0.5 V. After a tiny amount of N-DMBI was spin-coated (0.25 wt.%, 3,000 rpm, 30 s), N-DMBI doped $MoS_2$ shows as a near metallic material, with the effect of gate dependence disappearing and the saturation $I_{ds}$ increasing by two orders of magnitude. The 2D sheet charge density ($n_{2D}$) can be calculated by following formula

$$n_{2D} = \frac{\sigma_{2D}}{q\mu} = \frac{I_d L}{V_d W q \mu} \quad (1)$$

where $\sigma_{2D}$ is the conductivity of the 2D sheet, $q$ is the electron charge, $\mu$ is the carrier mobility, $L$ and $W$ are the channel length and width. The carrier mobility ($\mu$) can be extracted from the formula

$$\mu = \frac{L}{W C_{ox} V_d} \times \frac{dI_d}{dV_g} \quad (2)$$

where $C_{ox} = 1 \times 10^8$ $F \cdot cm^{-2}$ is the capacitance per unit area of 300 nm $SiO_2$ obtained from the parallel-plate capacitor model. Based on the statistical analysis of 20 $MoS_2$ FETs before and after N-MDBI doping (Fig. S5 in the ESM), average $n_{2D}$ value of the $MoS_2$ sheet increases from $1.66 \times 10^{11}$ to $4.02 \times 10^{13}$ $cm^{-2}$, which is consistent with the result of degenerate doping. This also suggests that N-DMBI is an extremely efficient n-type dopant on single-layer $MoS_2$, where a tiny amount can lead to a dramatic change in charge carrier density (more information about different concentrations of N-DMBI solution doping on $MoS_2$ is shown in Fig. S6 in the ESM). To modulate the doping concentration, N-DMBI doped $MoS_2$ FETs were immersed in clean chlorobenzene solvent so as the dopants can be controllably dissolved and partially washed away (Fig. 2(i)). The doping effect gradually decreases as seen from the evolution of charge density (Fig. S7 in the ESM). The air stability of the N-DMBI doped $MoS_2$ FETs was further measured (Fig. S8 in the ESM). Similar to most organic dopants, the charge density of N-DMBI doped $MoS_2$ keeps decreasing in air until it returns to initial state before doping, which seems n-doping effect of $MoS_2$ is weakened or even eliminated after exposed in air. These slowly varied N-DMBI doped $MoS_2$ FETs can be regenerated by annealing in $N_2$ glove box, where the $I_{ds}$ increases sharply again. This is presumably due to the removal of $O_2$ in air, indicating that proper encapsulation on N-DMBI doped $MoS_2$ can help retain the doping behavior in air.

In addition to enrich the carrier density of $MoS_2$, another challenge to achieve stretchable photodetectors with enhanced performance is to transfer integrable $MoS_2$ devices assembly onto elastomeric polymer. Current way to transfer microelectronic devices onto flexible substrates mainly refers to the sacrificial layer method [40, 41]. Prior to building devices with traditional lithography techniques, a sacrificial layer is firstly spin-coated on a rigid substrate, such as poly (vinyl alcohol) (PVA) and polyimide (PI). When the whole device is transferred onto the target substrate, another polymer layer, such as PMMA, is needed as supporting layer. Different solvents are used to dissolve the sacrificial layer and the supporting layer. In our case, to preserve the N-DMBI doping effect and the integrity of elastomer, many organic solvents are prohibited. To conquer the transfer challenges, we specifically chose transparent, stretchable thermoplastic elastomer SEBS to encapsulate the device assembly and "peel them off" from the $SiO_2$/Si substrate in one-step. N-DMBI could be sandwiched between $MoS_2$ and SEBS and isolated from air (as shown in Fig. 3(a)). Figure 3(b) shows the fabrication

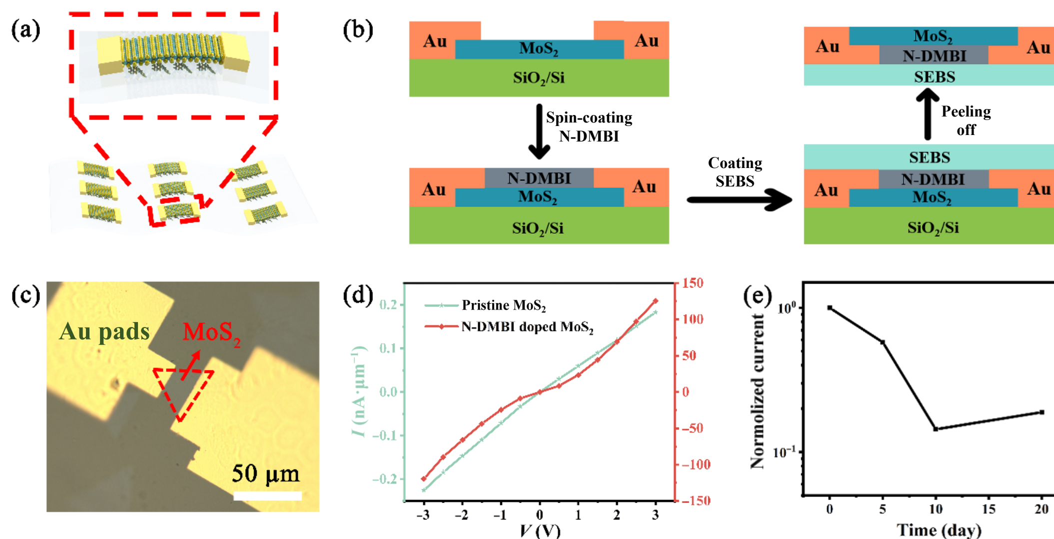


**Figure 3** Transfer of integrable N-DMBI doped $MoS_2$ device assembly onto elastomeric polymer. (a) Schematic illustration of N-DMBI doped $MoS_2$ devices on SEBS. N-DMBI could be preserved between $MoS_2$ and SEBS. (b) Schematic diagram of the transferred process of N-DMBI doped single-layer $MoS_2$ with Au electrodes from the $SiO_2$/Si rigid substrate to the SEBS elastomeric substrate. (c) Optical images of N-DMBI doped single-layer $MoS_2$ with Au electrodes transferred onto the SEBS substrate. (d) Comparison of $I$–$V$ curves of pristine and N-DMBI doped $MoS_2$ devices on SEBS. (e) Current evolution of N-DMBI doped $MoS_2$ stretchable device as a function of time exposed in air.

process of transferring integrable N-DMBI doped $MoS_2$ device assembly on SEBS. Starting from previously fabricated N-DMBI doped $MoS_2$ transistors on a $SiO_2$/Si substrate, SEBS film with fresh surface was closely laminated on the top of the transistors. To separate the devices encapsulated in SEBS with the underlying $SiO_2$/Si substrate, the whole assembly was next "peeled off" in alkaline solution to etch off $SiO_2$. Figure 3(c) shows a representative N-DMBI doped $MoS_2$ device transferred from the $SiO_2$/Si substrate on an elastomer. Raman was applied to confirm the successful transfer of $MoS_2$ (Fig. S9 in the ESM). Figure 3(d) plots the $I$–$V$ curves of pristine and N-DMBI doped $MoS_2$ devices on SEBS. Although there is a current decrease induced by trap states in SEBS [42, 43], the almost linear curves still exhibit good contact between $MoS_2$ and Au electrodes. Moreover, the current of N-DMBI doped $MoS_2$ is three orders of magnitude higher than that of pristine $MoS_2$. N-doping helps improve contact between the gold electrodes and $MoS_2$, decreasing contact resistances. And the width of Schottky barrier becomes thinner after n-doping, which allows electrons cross the metal-semicondutor junctions not only by thermoionic emission but also by tunneling (Fig. S10 in the ESM) [44]. The result also indicates N-DMBI doping effect is retained. In addition, the current of N-DMBI doped $MoS_2$ on SEBS was also monitored as a function of time exposed to air (Fig. 3(e)). Notably, the current of N-DMBI doped $MoS_2$ dropped by no more than one order of magnitude in 20 days. The small current drop can be attributed to the adsorption of oxygen on the surface of $MoS_2$. The relatively stable trend in the current of N-DMBI doped $MoS_2$ through SEBS transfer indicates that SEBS not only serves as a transfer medium and elastomeric substrate, but also encapsulates N-DMBI on $MoS_2$ and protects N-DMBI from oxidization by reaction with oxygen.

To explore the effect of N-DMBI dopants on the photoelectric characteristics after device assembly transfer, the optoelectronic performances of $MoS_2$ devices on SEBS were characterized with external optical excitation. Figure 4(a) displays the schematic diagram of a $MoS_2$-based stretchable photodetector. Both pristine and N-DMBI doped $MoS_2$ devices on SEBS show photosensitivity to external optical excitation from their $I$–$V$ curves acquired under dark and different optical power densities (Fig. 4(b) and Fig. S11 in the ESM). The photocurrent of N-DMBI doped $MoS_2$ devices (N-photodetector) is substantially larger than that of pristine $MoS_2$ devices, almost 25 times higher at $V$ = 3 V, $P$ = 3 mW·cm$^{-2}$ (Fig. 4(c)). The effect of N-DMBI doping on the optoelectronic performances of $MoS_2$ photodetectors on SEBS was further quantified by responsivity ($R$), detectivity ($D^*$) and photoresponse speed, which are figure-of-merits of photodetectors. $R$ is defined as

$$R = \frac{I_{ph}}{P \times S} \tag{3}$$

where $I_{ph}$ represents the photocurrent, which is equal to $I_{illumination} - I_{dark}$, $P$ represents the power density of light and $S$ represents the active illumination area. $D^*$ is defined as

$$D^* = R\sqrt{S/2eI_{dark}} \tag{4}$$

Based on statistical calculation, responsivity and detectivity as a function of power density are plotted in Figs. 4(d) and 4(e). Responsivity and detectivity of N-photodetectors show orders of magnitude improvement over the detected power density, which confirm that N-DMBI doping can enhance photoresponsivity of $MoS_2$ photodetectors. Specifically, the highest responsivity of N-photodetector is up to 738.2 A·W$^{-1}$ at $V$ = 3 V, light wavelength = 530 nm, $P$ = 0.01 mW·cm$^{-2}$, which is nearly 92 times higher than that of pristine $MoS_2$ photodetector. And the detectivity of N-photodetector can reach as high as 1.3 × 10$^{11}$ Jones, which is 4 times higher than that of pristine $MoS_2$ photodetector upon same illumination. These performances are very competitive among the $MoS_2$ flexible photodetectors (see comparison in the Table 1 and Table S1 in the ESM). While illumination power density increases, responsivity and detectivity of both N- and pristine $MoS_2$ photodetectors decrease, which can be attributed to the saturated formation and recombination of hole–electron pairs at high light intensity [48]. The quantitative relationship between responsivity and power density can be fitted by $R \propto P^{\alpha-1}$, where $\alpha$ values are 0.68 for pristine $MoS_2$ photodetector and 0.59 for N-photodetector. This indicates that both photoconductive (PC) and photogating (PG) effects contribute to the photocurrent, and PG effect plays a major role in enhanced photocurrent ($\Delta\alpha < 0$) [49–51]. In terms of photoresponse speed, N-photodetector based on N-DMBI doping exhibits relatively larger rise and decay time (Fig. S12 in the ESM). The response time of the N-DMBI doped $MoS_2$ device is 66 s, and the recovery time is 144 s. The slower response speed in N-

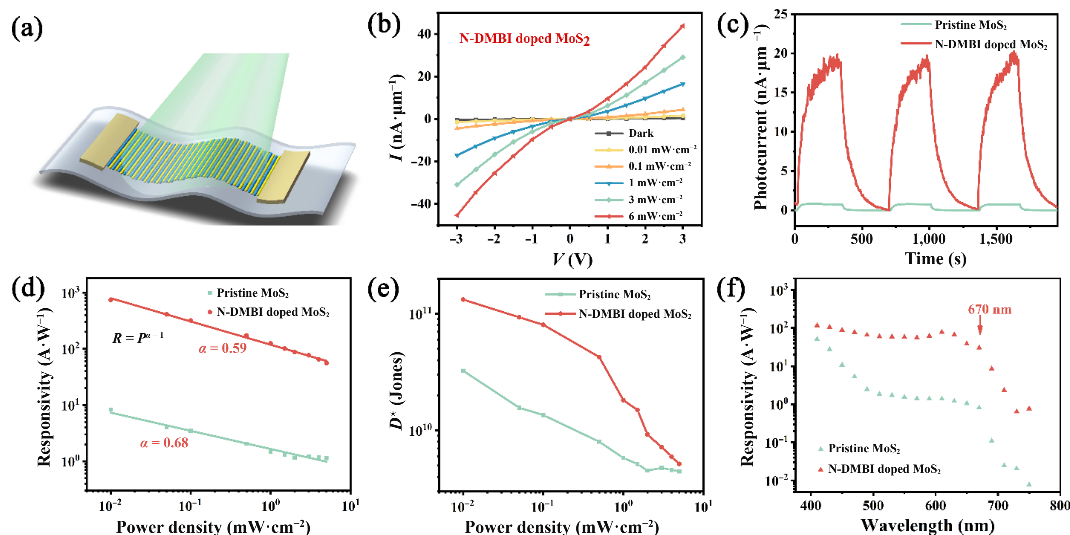


**Figure 4** Optoelectronic characteristics of $MoS_2$ photodetectors on SEBS. (a) Schematic illustration of a stretchable $MoS_2$-based photodetector. (b) $I$–$V$ curves for the N-DMBI doped $MoS_2$ photodetector (N-photodetector in short) under the dark and different optical power density. Light wavelength is 530 nm. (c) The time-resolved photocurrent for the N-photodetector and pristine $MoS_2$ photodetector upon light being turned on and off ($V$ = 3 V, $P$ = 3 mW·cm$^{-2}$, light wavelength is 530 nm). (d) Power density dependence of photoresponsivity and (e) detectivity for the N-photodetector and pristine $MoS_2$ photodetector at $V$ = 3 V, light wavelength is 530 nm. (f) Wavelength dependence of photoresponsivity for the N-photodetector and pristine photodetector at $V$ = 3 V, $P$ = 3 mW·cm$^{-2}$.

**Table 1** Performance comparison of our $MoS_2$ devices with other reported TMDs materials-based devices

| Material[a] | Responsivity (A·W$^{-1}$) | Operation | Flexible substrate | Transparent or not[b] | Stretchable or not[b] | Reference |
|---|---|---|---|---|---|---|
| S-$MoS_2$ | 5.5 | (642 nm; $P = 10^{-4}$ W; $V_{gs}$ = −1 V, $V_{ds}$ = 0.1 V) | PET | Y | N | [12] |
| Amorphous M-$MoS_2$ | Photocurrent ~ 0.1 nA | ($P$ = 12.5 mW·cm$^{-2}$; $V_{ds}$ = 20 V) | PI | N | N | [45] |
| Crystalline S-$MoS_2$ | 3.5 | (520 nm; $P = 6 \times 10^{-5}$ W; $V_{gs}$ = −1 V, $V_{ds}$ = 1 V) | PET | Y | N | [14] |
| Crystalline M-$MoS_2$ | $2.52 \times 10^{-6}$ | (515.6 nm; $P$ = 4.71–59.8 W·cm$^{-2}$; $V_{ds}$ = 1 V) | PDMS | Y | Y | [46] |
| Crystalline S-$MoS_2$ | 1.48 ± 0.03 | (450 nm; $V_{ds}$ = 1 V) | PET | Y | N | [47] |
| Crystalline S-$WS_2$ | $2.52 \times 10^{-3}$ | (532 nm; $P$ = 0.07 mW·cm$^{-2}$; $V_{ds}$ = 10 V) | PI | N | N | [57] |
| $WS_2$ | $1.09 \times 10^{-3}$ | (635 nm; $P$ = 10.7 mW·cm$^{-2}$; $V_{ds}$ = 10 V) | PI | N | N | [58] |
| $MoS_2$ nanosheets | $8.45 \times 10^{-6}$ | (660 nm; $P$ = 3.678 mW·cm$^{-2}$; $V_{ds}$ = 1 V) | Muscovite mica | Y | N | [59] |
| $WSe_2$ flake | 2.46 | (650 nm; $P$ = 8.1 mW·cm$^{-2}$; $V_{ds}$ = 0.1 V) | PI | N | N | [60] |
| $SnS_2$ | $44.5 \times 10^{-3}$ | (405 nm; $V_{ds}$ =4.5 V) | PI | N | N | [61] |
| $MoS_2$ microspheres | 0.963 | (405 nm; $P$ = 1.77 mW·cm$^{-2}$; $V_{ds}$ = 1 V) | PET | N | N | [62] |
| SnTe nanoflakes | 71.11 | (254 nm; $V_{ds}$ = 1 V) | PET | N | N | [63] |
| MOVPE-$MoS_2$ film | 920 | (532 nm; $P$ = 1 mW·cm$^{-2}$; $V_{gs}$ = 4 V, $V_{ds}$ = 2 V) | PI | N | N | [64] |
| Crystalline S-$MoS_2$ | 738.2 | (530 nm; $P$ = 0.01 mW·cm$^{-2}$; $V_{ds}$ = 3 V) | SEBS | Y | Y | This work |

[a]S stands for single-layer and M stands for multi-layer; [b]Y stands for yes and N stands for no.

photodetector agrees with the works about n-type doping on rigid substrates [51]. N-doping changes energy bands bending and the built-in potential near the metal-semiconductor junction, promoting the separation of photogenerated electron–hole pairs, further increasing the carrier density and photocurrent (Fig. S13 in the ESM) [13, 52]. The photoresponse behaviors of $MoS_2$ devices on SEBS were also tested with other illuminated wavelengths (Fig. 4(f)). Wavelength-dependence of responsivity shows an abrupt drop at a wavelength of 670 nm, which is related to direct band gap of $MoS_2$ (about 1.8 eV). The enhanced responsivity of N-photodetector across this illumination region again confirms that N-DMBI doping is an efficient way to enrich electron density so as to achieve photodetectors with high photoresponsivity.

To evaluate the strain-dependent performances of N-photodetectors on SEBS, we monitored its photoresponse behaviors as a function of tensile strain. The whole device on SEBS was fixed on a home-made stretching machine (Fig. S14 in the ESM) and its photoresponse was tested when the device was stretched both parallel and perpendicular to the direction of current flow (Figs. 5(a) and 5(b)). At parallel strain less than 5%, the photocurrent changes slowly with a normalized current change gradually approaching 0.1, and afterwards the changing slope becomes sharp. As a comparison, when the strain is perpendicular to the current flow, the critical strain at normalized current change of 0.1 can reach ~ 10%. Photocurrent changes under cyclic strain loading was also investigated. It can be seen within their critical strains their photoresponses upon optical irradiation are stable (Figs. 5(c) and 5(d)). To interpret the strain tolerance of N-photodetectors, we observed the morphology changes of $MoS_2$. Similar to graphene, single-layer $MoS_2$ is flexible at bending, but will form into cracks at stretching when the chemical bonding is destroyed [8, 9], as seen in Figs. 5(e) and 5(f). In order to observe their cracks clearly, N-photodetectors were stretched at ~ 100% strain parallel or perpendicular to the direction of current flow (Fig. S15 in the ESM). Despite of the crack propagation, electrons can still flow through percolating

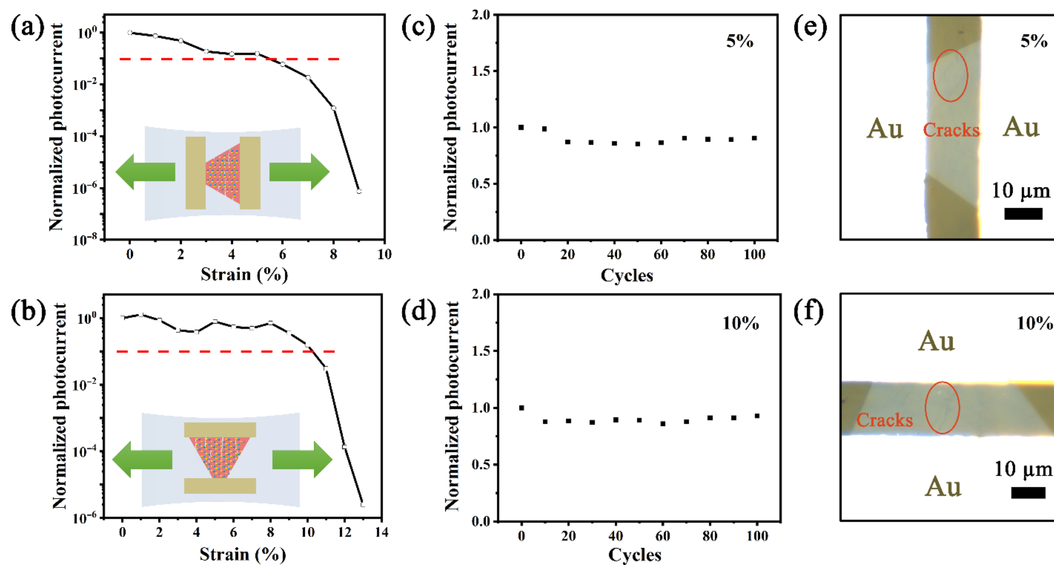


**Figure 5** Strain-dependent photoresponses of $MoS_2$ photodetectors on SEBS. Normalized photocurrent variation of N-photodetector as a function of strain both (a) parallel and (b) perpendicular to the direction of current flow. Normalized photocurrent variation of N-photodetectors as a function of cycle numbers under cyclic parallel and perpendicular strain loading up to (c) 5% and (d) 10% respectively. All photodetectors are measured at $V$ = 3 V, light wavelength = 530 nm, $P$ = 0.01 mW·cm$^{-2}$. Optical images of N-photodetector after 5% strain applied parallel to the direction of current flow (e) and 10% strain applied perpendicular to the direction of current flow (f). Representative cracks were labeled in the pictures.

pathways where $MoS_2$ is connected and the detector shows photoresponse upon illumination before complete breakage. When the orientation of cracks is parallel to the direction of current flow (inset of Figs. 5(a) and 5(b)), it is less effective for the photoresponse than perpendicular direction. Therefore, the ability of N-photodetectors on SEBS to maintain high photoresponse at certain strain can be attributed to the existence of percolating pathways upon stretching. The strain tolerance of this photodetector on SEBS can be further enhanced by transferring device assembly onto a pre-stretched SEBS or pre-patterning $MoS_2$ into curved structures, such as serpentine or coils [53–56].

## 4 Conclusion

In summary, we have demonstrated a high-photoresponsivity, air-stable and stretchable $MoS_2$ photodetector that benefits from the controllable modulation over the carrier concentration of $MoS_2$ via charge transfer at $MoS_2$ and N-DMBI interfaces, as well as the ability of elastic substrate SEBS to directly transfer the entire device. Direct transfer technology can avoid the use of organic solvents and encapsulate dopants to ensure the maintenance of doping effects. The increased carrier density greatly promotes carrier injection efficiency and photogenerated electron–hole separation efficiency at the metal–semiconductor interface, thus offering a significantly enhanced photoresponsivity in $MoS_2$ photodetectors. As-fabricated N-DMBI doped $MoS_2$ photodetector on SEBS exhibits a high responsivity of 738.2 A·W$^{-1}$ and detectivity of 1.3 × 10$^{11}$ Jones at $V$ = 3 V, light wavelength = 530 nm, $P$ = 0.01 mW·cm$^{-2}$, which are about 92 and 4 times higher than those of pristine $MoS_2$. Moreover, this photodetector can maintain a high photocurrent at a strain as high as 5% when stretched parallel to the direction of current flow and 10% when stretched perpendicular to the direction of current flow, which denotes the best stretchable photodetector based on single-layer $MoS_2$ so far. Our work provides a feasible way to achieve high-performance stretchable microelectronic devices of 2D materials.

## Acknowledgements

This work was supported by the National Natural Science Foundation of China (Nos. 21903007 and 22072006), Young Thousand Talents Program (No. 110532103), Beijing Normal University Startup funding (No. 312232102), Beijing Municipal Science & Technology Commission (No. Z191100000819002) and the Fundamental Research Funds for the Central Universities (No. 310421109). The authors also thank Prof. Liying Jiao from Tsinghua University for fruitful discussions and Prof. Hailin Peng and Prof. Yanfeng Zhang from Peking University for technical support.

**Electronic Supplementary Material**: Supplementary material (statistics of carrier density of $MoS_2$ FETs before and after N-DMBI doping, $n_{2D}$ evolution of the $MoS_2$ film as immersion time increased, representative transfer curves of $MoS_2$ FETs with different N-DMBI concentration, air stability of the N-DMBI doped $MoS_2$ FET, optical image and Raman spectra of N-DMBI doped $MoS_2$ with Au electrodes transferred on the SEBS substrate, band alignment at the $MoS_2$-Au junction before and after N-DMBI doping, photoelectric measurement of the pristine $MoS_2$ photodetector, photoresponse speed, schematic diagrams of band alignment at the pristine $MoS_2$-Au junction and N-DMBI doped $MoS_2$-Au junction under dark or illumination, optical image of the home-made stretching table, and optical images of N-photodetector after 100% strain applied parallel or perpendicular to the direction of current flow) is available in the online version of this article at https://doi.org/10.1007/s12274-022-4146-4.

## References

[1] Ko, H. C.; Stoykovich, M. P.; Song, J. Z.; Malyarchuk, V.; Choi, W. M.; Yu, C. J.; Geddes III, J. B.; Xiao, J. L.; Wang, S. D.; Huang, Y. G. et al. A hemispherical electronic eye camera based on compressible silicon optoelectronics. *Nature* **2008**, *454*, 748–753.

[2] Kim, J.; Kim, J.; Jo, S.; Kang, J. G.; Jo, J. W.; Lee, M.; Moon, J.; Yang, L.; Kim, M. G.; Kim, Y. H. et al. Ultrahigh detective heterogeneous photosensor arrays with In-pixel signal boosting capability for large-area and skin-compatible electronics. *Adv. Mater.* **2016**, *28*, 3078–3086.

[3] Koppelhuber, A.; Bimber, O. LumiConSense: A transparent, flexible, and scalable thin-film sensor. *IEEE Comput. Graph. Appl.* **2014**, *34*, 98–102.

[4] Lee, M. E.; Armani, A. M. Flexible UV exposure sensor based on UV responsive polymer. *ACS Sens.* **2016**, *1*, 1251–1255.

[5] Chen, S.; Lou, Z.; Chen, D.; Shen, G. Z. An artificial flexible visual memory system based on an UV-motivated memristor. *Adv. Mater.* **2018**, *30*, 1705400.

[6] Wang, S. H.; Xu, J.; Wang, W. C.; Wang, G. J. N.; Rastak, R.; Molina-Lopez, F.; Chung, J. W.; Niu, S. M.; Feig, V. R.; Lopez, J. et al. Skin electronics from scalable fabrication of an intrinsically stretchable transistor array. *Nature* **2018**, *555*, 83–88.

[7] Wang, S. H; Oh, J. Y.; Xu, J.; Tran, H.; Bao, Z. N. Skin-inspired electronics: An emerging paradigm. *Acc. Chem. Res.* **2018**, *51*, 1033–1045.

[8] Bertolazzi, S.; Brivio, J.; Kis, A. Stretching and breaking of ultrathin $MoS_2$. *ACS Nano* **2011**, *5*, 9703–9709.

[9] Zhang, W. F.; Zhang, Y.; Qiu, J. K.; Zhao, Z. H.; Liu, N. Topological structures of transition metal dichalcogenides: A review on fabrication, effects, applications, and potential. *InfoMat* **2021**, *3*, 133–154.

[10] Koppens, F. H. L.; Mueller, T.; Avouris, P.; Ferrari, A. C.; Vitiello, M. S.; Polini, M. Photodetectors based on graphene, other two-dimensional materials and hybrid systems. *Nat. Nanotechnol.* **2014**, *9*, 780–793.

[11] Choi, C.; Choi, M. K.; Liu, S. Y.; Kim, M. S.; Park, O. K.; Im, C.; Kim, J.; Qin, X. L, ; Lee, G. J.; Cho, K. W. et al. Human eye-inspired soft optoelectronic device using high-density $MoS_2$-graphene curved image sensor array. *Nat. Commun.* **2017**, *8*, 1664.

[12] De Fazio, D.; Goykhman, I.; Yoon, D.; Bruna, M.; Eiden, A.; Milana, S.; Sassi, U.; Barbone, M.; Dumcenco, D.; Marinov, K. et al. High responsivity, large-area graphene/$MoS_2$ flexible photodetectors. *ACS Nano* **2016**, *10*, 8252–8262.

[13] Pak, S.; Jang, A. R.; Lee, J.; Hong, J.; Giraud, P.; Lee, S.; Cho, Y.; An, G. H.; Lee, Y. W.; Shin, H. S. et al. Surface functionalization-induced photoresponse characteristics of monolayer $MoS_2$ for fast flexible photodetectors. *Nanoscale* **2019**, *11*, 4726–4734.

[14] Sun, B.; Shi, T. L.; Liu, Z. Y.; Wu, Y. N.; Zhou, J. X.; Liao, G. L. Large-area flexible photodetector based on atomically thin $MoS_2$/graphene film. *Mater. Des.* **2018**, *154*, 1–7.

[15] Fang, H.; Tosun, M.; Seol, G.; Chang, T. C.; Takei, K.; Guo, J.; Javey, A. Degenerate n-doping of few-layer transition metal dichalcogenides by potassium. *Nano Lett.* **2013**, *13*, 1991–1995.

[16] Kiriya, D.; Tosun, M.; Zhao, P. D.; Kang, J. S.; Javey, A. Air-stable surface charge transfer doping of $MoS_2$ by benzyl viologen. *J. Am. Chem. Soc.* **2014**, *136*, 7853–7856.

[17] Huang, Y.; Zhuge, F.; Hou, J. X.; Lv, L.; Luo, P.; Zhou, N.; Gan, L.; Zhai, T. Y. Van der Waals coupled organic molecules with monolayer $MoS_2$ for fast response photodetectors with gate-tunable responsivity. *ACS Nano* **2018**, *12*, 4062–4073.

[18] Zhao, Y. D.; Bertolazzi, S.; Samorì, P. A universal approach toward light-responsive two-dimensional electronics: Chemically tailored hybrid van der Waals heterostructures. *ACS Nano* **2019**, *13*, 4814–4825.

[19] Ji, H. G.; Solís-Fernández, P.; Yoshimura, D.; Maruyama, M.; Endo, T.; Miyata, Y.; Okada, S.; Ago, H. Chemically tuned p- and n-type $WSe_2$ monolayers with high carrier mobility for advanced electronics. *Adv. Mater.* **2019**, *31*, 1903613.

[20] Guo, R.; Li, Q.; Zheng, Y.; Lei, B.; Sun, H. C.; Hu, Z. H.; Zhang, J. L.; Wang, L.; Longhi, E.; Barlow, S. et al. Degenerate electron-doping in two-dimensional tungsten diselenide with a dimeric organometallic reductant. *Mater. Today* **2019**, *30*, 26–33.

[21] Sun, J. C.; Wang, Y. Y.; Guo, S. Q.; Wan, B. S.; Dong, L. Q.; Gu, Y. D.; Song, C.; Pan, C. F.; Zhang, Q. H.; Gu, L. et al. Lateral 2D $WSe_2$ p-n homojunction formed by efficient charge-carrier-type modulation for high-performance optoelectronics. *Adv. Mater.* **2020**, *32*, 1906499.

[22] Zhu, X. Q.; Zhang, M. T.; Yu, A.; Wang, C. H.; Cheng, J. P. Hydride, hydrogen atom, proton, and electron transfer driving forces of various five-membered heterocyclic organic hydrides and their reaction intermediates in acetonitrile. *J. Am. Chem. Soc.* **2008**, *130*, 2501–2516.

[23] Kresse, G.; Furthmüller, J. Efficient iterative schemes for *ab initio* total-energy calculations using a plane-wave basis set. *Phys. Rev. B* **1996**, *54*, 11169–11186.

[24] Ernzerhof, M.; Scuseria, G. E. Assessment of the Perdew-Burke-Ernzerhof exchange-correlation functional. *J. Chem. Phys.* **1999**, *110*, 5029–5036.

[25] Kresse, G.; Joubert, D. From ultrasoft pseudopotentials to the projector augmented-wave method. *Phys. Rev. B* **1999**, *59*, 1758–1775.

[26] Grimme, S.; Antony, J.; Ehrlich, S.; Krieg, H. A consistent and accurate *ab initio* parametrization of density functional dispersion correction (DFT-D) for the 94 elements H-Pu. *J. Chem. Phys.* **2010**, *132*, 154104.

[27] Zhao, Y.; Truhlar, D. G. The M06 suite of density functionals for main group thermochemistry, thermochemical kinetics, noncovalent interactions, excited states, and transition elements: Two new functionals and systematic testing of four M06-class functionals and 12 other functionals. *Theor. Chem. Acc.* **2008**, *120*, 215–241.

[28] Zeng, Y.; Zheng, W. Y.; Guo, Y.; Han, G. C.; Yi, Y. P. Doping mechanisms of N-DMBI-H for organic thermoelectrics: Hydrogen removal vs. hydride transfer. *J. Mater. Chem. A* **2020**, *8*, 8323–8328.

[29] Monkhorst, H. J.; Pack, J. D. Special points for Brillouin-zone integrations. *Phys. Rev. B* **1976**, *13*, 5188–5192.

[30] Wei, P.; Oh, J. H.; Dong, G. F.; Bao, Z. N. Use of a 1*H*-benzoimidazole derivative as an *n*-type dopant and to enable air-stable solution-processed *n*-channel organic thin-film transistors. *J. Am. Chem. Soc.* **2010**, *132*, 8852–8853.

[31] Kwon, S. J.; Han, T. H.; Kim, Y. H.; Ahmed, T.; Seo, H. K.; Kim, H.; Kim, D. J.; Xu, W. T.; Hong, B. H.; Zhu, J. X. et al. Solution-processed n-type graphene doping for cathode in inverted polymer light-emitting diodes. *ACS Appl. Mater. Interfaces* **2018**, *10*, 4874–4881.

[32] Chee, S. S.; Lee, W. J.; Jo, Y. R.; Cho, M. K.; Chun, D.; Baik, H.; Kim, B. J.; Yoon, M. H.; Lee, K.; Ham, M. H. Atomic vacancy control and elemental substitution in a monolayer molybdenum disulfide for high performance optoelectronic device arrays. *Adv. Funct. Mater.* **2020**, *30*, 1908147.

[33] Chakraborty, B.; Bera, A.; Muthu, D. V. S.; Bhowmick, S.; Waghmare, U. V.; Sood, A. K. Symmetry-dependent phonon renormalization in monolayer $MoS_2$ transistor. *Phys. Rev. B* **2012**, *85*, 161403.

[34] Lin, J. D.; Han, C.; Wang, F.; Wang, R.; Xiang, D.; Qin, S. Q.; Zhang, X. A.; Wang, L.; Zhang, H.; Wee, A. T. S. et al. Electron-doping-enhanced trion formation in monolayer molybdenum disulfide functionalized with cesium carbonate. *ACS Nano* **2014**, *8*, 5323–5329.

[35] Zhang, S. Y.; Hill, H. M.; Moudgil, K.; Richter, C. A.; Hight Walker, A. R.; Barlow, S.; Marder, S. R.; Hacker, C. A.; Pookpanratana, S. J. Controllable, wide-ranging n-doping and p-doping of monolayer group 6 transition-metal disulfides and diselenides. *Adv. Mater.* **2018**, *30*, 1802991.

[36] Mak, K. F.; He, K. L.; Lee, C. G.; Lee, G. H.; Hone, J.; Heinz, T. F.; Shan, J. Tightly bound trions in monolayer $MoS_2$. *Nat. Mater.* **2013**, *12*, 207–211.

[37] Heo, K.; Jo, S. H.; Shim, J.; Kang, D. H.; Kim, J. H.; Park, J. H. Stable and reversible triphenylphosphine-based n-type doping technique for molybdenum disulfide ($MoS_2$). *ACS Appl. Mater. Interfaces* **2018**, *10*, 32765–32772.

[38] Lien, D. H.; Uddin, S. Z.; Yeh, M.; Amani, M.; Kim, H.; Ager III, J. W.; Yablonovitch, E.; Javey, A. Electrical suppression of all nonradiative recombination pathways in monolayer semiconductors. *Science* **2019**, *364*, 468–471.

[39] Tarasov, A.; Zhang, S. Y.; Tsai, M. Y.; Campbell, P. M.; Graham, S.; Barlow, S.; Marder, S. R.; Vogel, E. M. Controlled doping of large-area trilayer $MoS_2$ with molecular reductants and oxidants. *Adv. Mater.* **2015**, *27*, 1175–1181.

[40] Tsai, M. Y.; Tarasov, A.; Hesabi, Z. R.; Taghinejad, H.; Campbell, P. M.; Joiner, C. A.; Adibi, A.; Vogel, E. M. Flexible $MoS_2$ field-effect transistors for gate-tunable piezoresistive strain sensors. *ACS Appl. Mater. Interfaces* **2015**, *7*, 12850–12855.

[41] Salvatore, G. A.; Münzenrieder, N.; Barraud, C.; Petti, L.; Zysset, C.; Büthe, L.; Ensslin, K.; Tröster, G. Fabrication and transfer of

flexible few-layers $MoS_2$ thin film transistors to any arbitrary substrate. *ACS Nano* **2013**, *7*, 8809–8815.

[42] Liu, Y.; Guo, J.; Zhu, E. B.; Liao, L.; Lee, S. J.; Ding, M. N.; Shakir, I.; Gambin, V.; Huang, Y.; Duan, X. F. Approaching the Schottky-Mott limit in van der Waals metal-semiconductor junctions. *Nature* **2018**, *557*, 696–700.

[43] Bao, W. Z.; Cai, X. H.; Kim, D.; Sridhara, K.; Fuhrer, M. S. High mobility ambipolar $MoS_2$ field-effect transistors: Substrate and dielectric effects. *Appl. Phys. Lett.* **2013**, *102*, 042104.

[44] Lee, S. Y.; Kim, U. J.; Chung, J.; Nam, H.; Jeong, H. Y.; Han, G. H.; Kim, H.; Oh, H. M.; Lee, H.; Kim, H. et al. Large work function modulation of monolayer $MoS_2$ by ambient gases. *ACS Nano* **2016**, *10*, 6100–6107.

[45] Lim, Y. R.; Song, W.; Han, J. K.; Lee, Y. B.; Kim, S. J.; Myung, S.; Lee, S. S.; An, K. S.; Choi, C. J.; Lim, J. Wafer-scale, homogeneous $MoS_2$ layers on plastic substrates for flexible visible-light photodetectors. *Adv. Mater.* **2016**, *28*, 5025–5030.

[46] Kim, R. H.; Leem, J.; Muratore, C.; Nam, S.; Rao, R.; Jawaid, A.; Durstock, M.; Mcconney, M.; Drummy, L.; Rai, R. et al. Photonic crystallization of two-dimensional $MoS_2$ for stretchable photodetectors. *Nanoscale* **2019**, *11*, 13260–13268.

[47] Pak, S.; Lee, J.; Jang, A. R.; Kim, S.; Park, K. H.; Sohn, J. I.; Cha, S. Strain-engineering of contact energy barriers and photoresponse behaviors in monolayer $MoS_2$ flexible devices. *Adv. Funct. Mater.* **2020**, *30*, 2002023.

[48] Buscema, M.; Groenendijk, D. J.; Blanter, S. I.; Steele, G. A.; Van Der Zant, H. S. J.; Castellanos-Gomez, A. Fast and broadband photoresponse of few-layer black phosphorus field-effect transistors. *Nano Lett.* **2014**, *14*, 3347–3352.

[49] Furchi, M. M.; Polyushkin, D. K.; Pospischil, A.; Mueller, T. Mechanisms of photoconductivity in atomically thin $MoS_2$. *Nano Lett.* **2014**, *14*, 6165–6170.

[50] Buscema, M.; Island, J. O.; Groenendijk, D. J.; Blanter, S. I.; Steele, G. A.; Van Der Zant, H. S. J.; Castellanos-Gomez, A. Photocurrent generation with two-dimensional van der Waals semiconductors. *Chem. Soc. Rev.* **2015**, *44*, 3691–3718.

[51] Fang, H. H.; Hu, W. D. Photogating in low dimensional photodetectors. *Adv. Sci.* **2017**, *4*, 1700323.

[52] Prades, J. D.; Hernandez-Ramirez, F.; Jimenez-Diaz, R.; Manzanares, M.; Andreu, T.; Cirera, A.; Romano-Rodriguez, A.; Morante, J. R. The effects of electron-hole separation on the photoconductivity of individual metal oxide nanowires. *Nanotechnology* **2008**, *19*, 465501.

[53] Zang, J. F.; Ryu, S.; Pugno, N.; Wang, Q. M.; Tu, Q.; Buehler, M. J.; Zhao, X. H. Multifunctionality and control of the crumpling and unfolding of large-area graphene. *Nat. Mater.* **2013**, *12*, 321–325.

[54] Kang, P.; Wang, M. C.; Knapp, P. M.; Nam, S. Crumpled graphene photodetector with enhanced, strain-tunable, and wavelength-selective photoresponsivity. *Adv. Mater.* **2016**, *28*, 4639–4645.

[55] Mu, J. K.; Hou, C. Y.; Wang, G.; Wang, X. M.; Zhang, Q. H.; Li, Y. G.; Wang, H. Z.; Zhu, M. F. An elastic transparent conductor based on hierarchically wrinkled reduced graphene oxide for artificial muscles and sensors. *Adv. Mater.* **2016**, *28*, 9491–9497.

[56] Bera, K. P.; Haider, G.; Usman, M.; Roy, P. K.; Lin, H. I.; Liao, Y. M.; Inbaraj, C. R. P.; Liou, Y. R.; Kataria, M.; Lu, K. L. et al. Trapped photons induced ultrahigh external quantum efficiency and photoresponsivity in hybrid graphene/metal-organic framework broadband wearable photodetectors. *Adv. Funct. Mater.* **2018**, *28*, 1804802.

[57] Lan, C. Y.; Zhou, Z. Y.; Zhou, Z. F.; Li, C.; Shu, L.; Shen, L. F.; Li, D. P.; Dong, R. T.; Yip, S.; Ho, J, C. Wafer-scale synthesis of monolayer $WS_2$ for high-performance flexible photodetectors by enhanced chemical vapor deposition. *Nano Res.* **2018**, *11*, 3371–3384.

[58] Kim, B. H.; Yoon, H.; Kwon, S. H.; Kim, D. W.; Yoon, Y. J. Direct $WS_2$ photodetector fabrication on a flexible substrate. *Vacuum* **2021**, *184*, 109950.

[59] Bao, Y. X.; Han, J. F.; Li, H. X.; Huang, K. Flexible, heat-resistant photodetector based on $MoS_2$ nanosheets thin film on transparent muscovite mica substrate. *Nanotechnology* **2021**, *32*, 025206.

[60] Ma, Y. F.; Liu, D.; Hao, J. X.; Wang, L.; Wang, W. High-performance flexible $WSe_2$ flake photodetector with broadband detection capability. *AIP Adv.* **2020**, *10*, 125027.

[61] Pradhan, N. R.; Garcia, C.; Holleman, J.; Rhodes, D.; Parker, C.; Talapatra, S.; Terrones, M.; Balicas, L.; McGill, S. A. Photoconductivity of few-layered p-$WSe_2$ phototransistors via multi-terminal measurements. *2D Mater.* **2016**, *3*, 041004.

[62] Lei, Y.; Luo, J.; Yang, X. G.; Cai, T.; Qi, R. J.; Gu, L. Y.; Zheng, Z. Thermal evaporation of large-area $SnS_2$ thin films with a UV-to-NIR photoelectric response for flexible photodetector applications. *ACS Appl. Mater. Interfaces* **2020**, *12*, 24940–24950.

[63] Han, J. F.; Li, J. Y.; Liu, W. L.; Li, H. X.; Fan, X. Y.; Huang, K. A novel flexible broadband photodetector based on flower-like $MoS_2$ microspheres. *Optics Commun.* **2020**, *473*, 125931.

[64] Yang, J.; Yu, W. Z.; Pan, Z. H.; Yu, Q.; Yin, Q.; Guo, L.; Zhao, Y. F.; Sun, T.; Bao, Q. L.; Zhang, K. Ultra-broadband flexible photodetector based on topological crystalline insulator SnTe with high responsivity. *Small* **2018**, *14*, 1802598.

[65] Schneider, D. S.; Grundmann, A.; Bablich, A.; Passi, V.; Kataria, S.; Kalisch, H.; Heuken, M.; Vescan, A.; Neumaier, D.; Lemme, M. C. Highly responsive flexible photodetectors based on MOVPE grown uniform few-layer $MoS_2$. *ACS Photonics* **2020**, *7*, 1388–1395.